# $^{16}$O breakup in quasielastic reactions near the Fermi energy

E. Chavez-Lomeli, A. Dacal, and M. E. Ortiz
*Instituto de Fisica, Universidad Nacional Autónoma de México, A. P. 20-364, Del A. Obregon, Mexico D. F., Mexico*

S. B. Gazes
*Nuclear Structure Research Laboratory, University of Rochester, Rochester, New York 14627*

Y. Chan and R. G. Stokstad
*Nuclear Science Division, Lawrence Berkeley Laboratory, Berkeley, California 94720*

E. Plagnol
*Grand Accelerateur National d'Ions Lourds (GANIL), 14021 Caen CEDEX, France*

K. Siwek-Wilczynska
*Institute of Experimental Physics, Warsaw University, 00-681 Warsaw, Poland*

J. Wilczynski
*Institute for Nuclear Studies, 05-400 Swierk-Otwock, Poland*
(Received 23 February 1993)

The quasielastic breakup of an $^{16}$O nucleus at 32.5 MeV/nucleon on a $^{197}$Au target has been investigated by measuring the projectilelike fragments in coincidence with the emitted light charged particles. It is found that the breakup proceeds via sequential, two-step processes in which inelastic scattering and one-neutron pickup are the most significant components in the formation of the primary fragment. This is followed by statistical decay of the highly excited primary fragment. A Monte Carlo simulation was used to identify these processes and to deduce differential and total cross sections for the breakup of $^{16}$O into the $\alpha$+$^{12,13}$C channels.

PACS number(s): 25.70.Bc, 27.20.+n

## I. INTRODUCTION

Nuclear reaction mechanisms have been studied for many years using "light" heavy-ion beams over a wide range of bombarding energies [1–4]. The mechanism for formation of projectilelike fragments (PLF) has been thought to evolve as a function of the bombarding energy. Near the interaction barrier, inelastic scattering and quasielastic transfer of one or a few nucleons occur while at relativistic energies a prompt nuclear fragmentation should dominate. For the intermediate energy range, between 20 and 100 MeV per nucleon, a strong competition is expected between high- and low-energy reaction mechanisms for the production of the PLF. One of the aims of the present work is to study their relative importance.

In the case of binary breakup, where only two fragments are produced from the original primary fragment (PF), it is possible to reconstruct the PF if both fragments are detected in coincidence. For "light" heavy ions, this breakup is usually via the emission of a light charged particle (LP) with $Z = 1$ or 2. Moreover, if the energy and direction of motion are measured, it is possible to reconstruct the whole breakup process and determine whether it is consistent with sequential decay. We will infer a prompt breakup only if there are experimental features that cannot be explained under the assumption of a sequential process.

In this paper, we present experimental results of a detailed study of PLF production in reactions induced by 520 MeV $^{16}$O projectiles on a $^{197}$Au target. The experiments were performed at the 88 Inch Cyclotron of Lawrence Berkeley Laboratory. Section II discusses the detection systems used during the experiments. Section III contains the results of the measurements. In Sec. IV we concentrate on kinematical reconstructions of primary fragments for the most abundant coincidence channels, discussing our results in relation to Monte Carlo simulations and model predictions. Finally the conclusions of the present work are found in Sec. V.

## II. EXPERIMENTAL SETUP

Two different detection configurations were used and are shown schematically in Figs. 1(a) and 1(b). In configuration 1 [Fig. 1(a)], a tightly collimated ($\pm 0.8°$) two-element solid-state silicon telescope fixed at 6° in the vertical plane determined the energy, charge, and mass of the PLF for $Z > 2$. A total of 12 plastic phoswich detectors [5, 6] were placed around the beam direction and

 

the PLF detector, covering a large fraction of the solid angle in the forward direction. Five of these phoswiches, the "slices," were $30 \times 2.5 \times 2.5$ cm$^3$ and the other seven, the "cubes," were $2.5 \times 2.5 \times 2.5$ cm$^3$. The NE115 slow plastic scintillator was preceded by a 1-mm-thick NE102 fast scintillator, which enabled energy measurement and charge identification for charged particles with $Z < 3$ [5–7]. Configuration 2 [Fig. 1(b)] is also a combination of a silicon telescope for the PLF detector and an array of phoswich detectors to observe the associated light charged particles (LP). The slices were oriented horizontally to allow the telescope (telescope 1) to move to different angles in the horizontal plane. This plane is not the same as the reaction plane defined in our analysis, which is the plane containing the beam and the primary fragment. A second telescope (telescope 2) was placed in the vertical plane, underneath the slices, fixed at 16°. Configuration 1 represents an effort to cover the largest possible fraction of the solid angle around the beam and the PLF detector in the forward direction. Configuration 2 was designed to investigate the dependence of the coincidence yield with PLF angle. Singles angular distributions for the PLF were also measured with this arrangement.

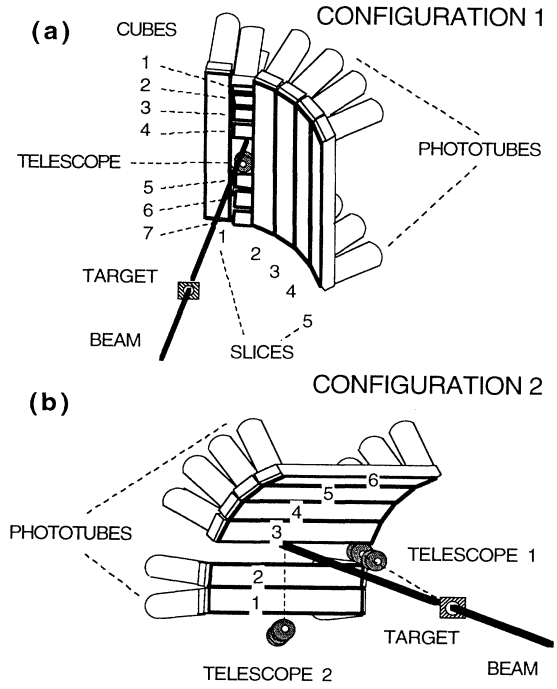


FIG. 1. Schematic representation of the experimental detection configurations. The two setups shown here are a combination of two element silicon solid state telescopes for the detection of PLFs and an array of phoswich detectors to detect the LPs in coincidence. The heavy lines around the phoswich detectors (cubes and slices) represent brass collimation used to stop particles with trajectories that would exit a detector side. The center of the slices in (a) was at 0° relative to the beam, while in configuration 2 it was at 5°, on the same side of the beam as the telescope 1. The telescope in (a) was fixed at 6°. The collimator in front defined the PLF angle to within 0.8°. In (b), telescope 1 could move on the horizontal plane and telescope 2 was fixed in the vertical plane at 16°. The collimation was the same as in (a).

For analysis, the position of the PLF was taken as the center of the telescope. The position of the LP was treated as follows: In the case of the cubes the position is taken as the center of the square collimator ( ± 10 mm ±3.2°) placed in front of the detector. This assumption results in discrete bins for the position spectrum, but the alternative procedure consisting of randomizing the position across the face of the detector [7] increases the uncertainty in the position measurement, which is critical in determining the relative energy between the PLF and LP, and for that reason was not used here.

The relative amount of light collected at each end of the slice detector gave position information for the long dimension [5,6]. The position resolution depended on the position of the LP, being best (2 mm) near the center of the detector and worst (3 mm) near the phototubes. In the transverse direction, the position is taken as the center of the detector with an uncertainty of half its active width ( ± 10 mm).

The combined energy and position information enabled reconstruction of the linear momentum vector of each particle. From these vectors we obtained the laboratory velocity of the center of mass of the PLF-LP system, and the relative velocity of the PLF and LP.

## III. RESULTS

### A. Inclusive measurements

Inclusive differential cross sections for the various PLF were measured in the angular range 4.5° to 18° in the laboratory system. Figure 2 shows angular distributions for the carbon isotopes. The exponential fall of the cross section with angle is a feature common to all PLF from beryllium to oxygen. In spite of the limited angular range, the angle-integrated cross sections have uncertainties smaller than 20%. Most of this uncertainty is associated with the extrapolation to 0°. Inclusive angle-

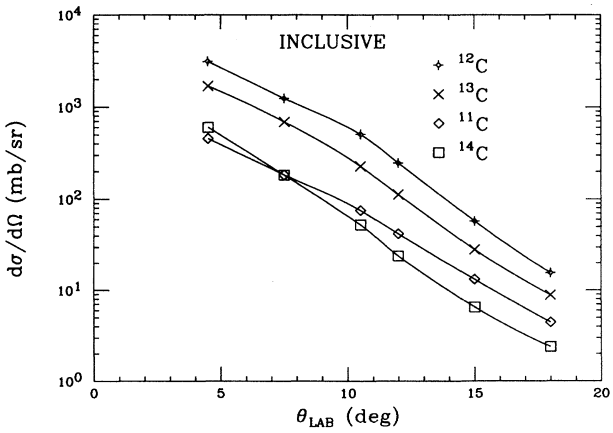


FIG. 2. Inclusive angular distribution for the PLFs as obtained with configuration 2. Carbon isotopes are shown. The nearly exponential falloff of the distribution is a characteristic common to all PLFs.

integrated cross sections are given in Table I, for several isotopes of PLFs with $3 < Z < 9$.

### B. Coincidence measurements

Table II shows the number of coincidence events obtained in configuration 2 with the PLF detector at 9° in order to illustrate the relative intensity of the different coincidence channels. Even though these numbers are not corrected for detection efficiency they give an idea of the general trends of the yields for different channels. Double coincidences (one LP in coincidence with a PLF) are about an order of magnitude more intense than triple coincidences. Therefore we will concentrate on the former and mainly on the most abundant channels.

Table III gives the relative yield for the four most abundant channels, $^{12}$C+$\alpha$, $^{13}$C+$\alpha$, $^{11}$B + $\alpha$, and $^{15}$N + $p$, obtained in configuration 2 for different angles of the silicon telescope.

To analyze these coincidence measurements we calculate $Q_3$ and $E_{\rm rel}$. The latter quantity is the relative kinetic energy of the PLF and LP, i.e., their total kinetic energy in the center of mass of their relative motion, while $Q_3$ is the inelasticity of the reaction

$$Q_3 = E(\text{LP}) + E(\text{PLF}) + E(\text{TLF}) - E(\text{beam}),$$

where $E$(TLF) is the kinetic energy of the targetlike fragment (TLF), deduced from momentum conservation.

#### 1. The $Q_3$ spectra

Figure 3 shows the $Q_3$ spectra for the four strongest coincidence channels. They have very different shapes. For the $^{12}$C + $\alpha$ and $^{13}$C + $\alpha$ channels [Figs. 3(a) and 3(b)], two distinct components can be identified: a quasielastic one at low $Q_3$ values, near the $Q$ value for production of the three bodies in their ground states, $Q_{ggg}$ (shown by arrows on the figure), and a second component at more negative $Q$ values. We will refer to these components as the $Q_{ggg}$ and the highly inelastic components. Other channels such as $^{11}$B + $\alpha$ [Fig. 3(c)] do not show the same structure—the $Q_{ggg}$ component is missing.

The highly inelastic component of the spectra on Fig. 3 can be associated with energy absorbed by the TLF in the form of intrinsic excitation since the products of its decay, being neutral or low-energy charged particles, will be undetected and thus the energy they carry will not be collected. This may be the case in the $^{13}$C and $^{11}$B + $\alpha$ channels as we will discuss. However, events in which particles from the PF are undetected will also populate this $Q_3$ region, since they will carry away energy. In the event that the detection efficiency for fragments of the PF is low, i.e., their escape probability is not negligible, the interpretation of this $Q_3$ region solely in terms of intrinsic excitation of the TLF is no longer possible. Moreover, for those cases, in the definition of $Q_3$, the term that accounts for the recoil energy of the TLF will have a different meaning.

When the sum of the masses and charges of the PLF and LP are equal to or larger than those of the projectile, no net transfer of mass to the target has taken place and no large excitation is expected in the TLF [7–10]. The enhanced yield in the highly inelastic region of the $^{12}$C + $\alpha$ channel, relative to the $^{13}$C+$\alpha$ one, has been attributed [11] to the formation of a primary $^{17}$O by a one-neutron pickup process followed by a double sequential decay ($n$-$\alpha$ or $\alpha$-$n$). The neutron always escapes detection and we cannot associate the missing energy to excitation of the TLF in the case of $^{12}$C + $\alpha$.

In the case of the $^{15}$N + $p$ channel [Fig. 3(d)], one might expect the same structure as for $^{12}$C + $\alpha$ if both detected particles come from the decay of $^{16}$O. The $Q_{ggg}$ peak in this case, however, is not clearly defined. We shall come back to discuss this feature when the sequential nature of the $Q_{ggg}$ peak in the carbon channels is demonstrated. For more negative $Q_3$ values we can argue that there is a similar highly inelastic "bump" as in the $^{12}$C + $\alpha$ case, and thus subject to the same interpretation.

In the $^{11}$B + $\alpha$ channel [Fig. 3(c)], the sum of the masses of the PLF and LP is smaller than the projectile, so the energy carried by the missing proton has not been collected. This explains the disappearence of the $Q_{ggg}$ peak here and, since our system is efficient for the detection of protons, it is likely that the proton has been captured by the target.

In the case of the $^{13}$C + $\alpha$ channel, additional undetected particles from the PF will correspond to pickup

TABLE I. Inclusive cross sections (mb).

| | | | |
|---|---|---|---|
| $^{17}$O | 47 | $^{12}$C | 220 |
| $^{16}$O[a] | 1100 | $^{11}$C | 34 |
| $^{15}$N | 140 | $^{11}$B | 140 |
| $^{14}$N | 100 | $^{10}$B | 60 |
| $^{13}$N | 50 | $^{10}$Be | 34 |
| $^{14}$C | 42 | $^{9}$Be | 47 |
| $^{13}$C | 120 | $^{7}$Be | 31 |

[a]Inelastic scattering.

TABLE II. Relative coincidence yields configuration 2, telescope at 9°.

| | $\alpha$ | $p$ | $p$-$\alpha$ | $\alpha$-$\alpha$ | $p$-$p$ |
|---|---|---|---|---|---|
| $^{15}$N | 16 | 1444 | 44 | 4 | 16 |
| $^{14}$N | 13 | 1194 | 51 | 5 | 21 |
| $^{13}$C | 2153 | 110 | 212 | 6 | 76 |
| $^{12}$C | 6713 | 283 | 455 | 19 | 111 |
| $^{11}$B | 3192 | 250 | 398 | 44 | 52 |

TABLE III. Relative yield from configuration 2, not corrected by detection efficiency.

| PLF angle (deg) | 4.5 | 6 | 9 | 12 | 16[a] |
|---|---|---|---|---|---|
| $^{12}$C+$\alpha$ | 334 | 247 | 108 | 34 | 2.4 |
| $^{13}$C+$\alpha$ | 98 | 79 | 30 | 9 | 0.8 |
| $^{11}$B+$\alpha$ | 155 | 112 | 46 | 17 | 2.3 |
| $^{15}$N+$p$ | 63 | 54 | 25 | 5 | 0.3 |

[a]Data from telescope 2.

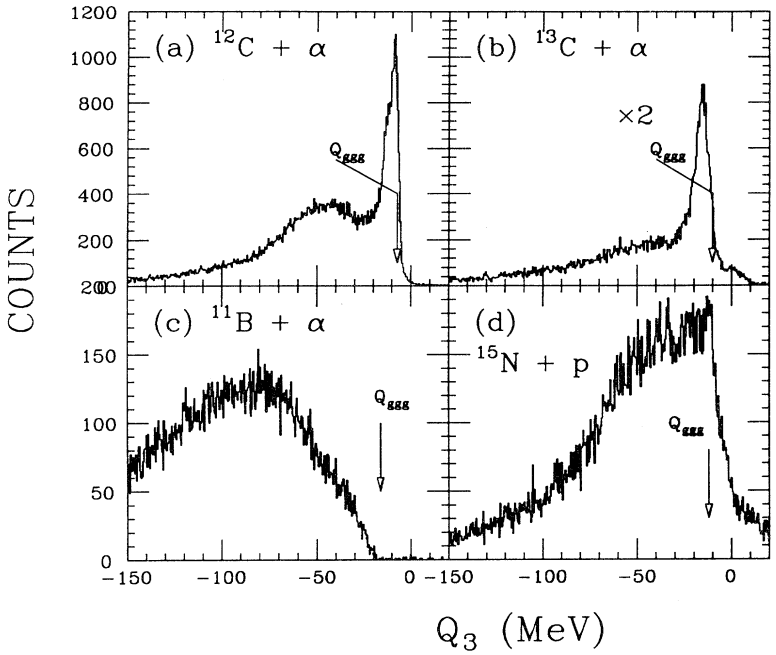


FIG. 3. $Q_3$ spectra of four different PLF-LP coincidence channels. The $Q$ value for production of the PLF, LP, and corresponding TLF in their ground states ($Q_{ggg}$) is shown with arrows. The quasielastic peaks in (a) and (b) are referred to as the "$Q_{ggg}$" peaks in the text.

reactions of at least two nucleons, yielding highly excited primary fragments. The number of channels available for the decay of such an excited nucleus increases and the probability to produce a bound $^{13}$C as a final product of the deexcitation process is smaller. In this case, as in the previous one, even though we cannot rule out completely the existence of events where nucleons from the PF are missing, the highly inelastic component may be mostly associated with intrinsic excitation energy in the TLF.

A characteristic feature of events in the $Q_{ggg}$ peak is that, since we have collected most of the available energy of the system (to within a few MeV), there is insufficient energy missing to have an additional undetected particle or fragment from the projectile. Thus, the identity of the PF can be deduced from the direct sum of the masses and charges of the PLF and LP. In the case of events in the $Q_{ggg}$ peak of the $^{12}$C + $\alpha$ and $^{13}$C + $\alpha$ channels we know that they come from the quasielastic breakup of primary $^{16}$O and $^{17}$O, respectively. This is not necessarily the case for events in the highly inelastic region.

### 2. *Sequential nature of the quasielastic breakup*

In the following we examine whether the assumption that breakup of the projectile proceeds via a sequential process is consistent with our data. In this picture the PLF and the associated LP are products of the decay of a PF formed at the moment when projectile and target interact. The case of the breakup of $^{16}$O into $^{12}$C + $\alpha$ is particularly relevant for this discussion because of the large energy gap between the breakup threshold (7.16 MeV) and the first excited state of $^{16}$O (9.6 MeV) [12]. This feature of the structure of $^{16}$O translates into the expectation that the relative kinetic energy ($E_{\rm rel}$) of the system $^{12}$C + $\alpha$ must be larger than 2.4 MeV. This minimum value introduces kinematical constraints on the energy and direction of the $\alpha$ particle when the $^{12}$C is detected in a given position. Figure 4 shows schematically this situation with velocity vectors for the decay of a PF with fixed excitation energy. The size of the center-of-mass velocity vectors of PLF and LP increases with the excitation energy of the PF (assuming both are emitted in their ground state). The minimum velocity vector determines the size of the sequentially forbidden sphere in this velocity space.

By restricting ourselves to data in the $Q_{ggg}$ peak of the $Q_3$ spectrum for $^{12}$C + $\alpha$ [see Fig. 3(a)], we guarantee that the identity of the PF is indeed $^{16}$O. Figure 5 shows two-dimensional plots of energy vs vertical position of $\alpha$ particles in coincidence with $^{12}$C gated on the $Q_{ggg}$ peak. Figures 5(b), 5(c), and 5(d) correspond to configuration 2 where alphas were detected in slice 3 [see Fig. 1(b)]. In this configuration, the center of the slice was located at 5° relative to the beam. $^{12}$C ions were detected at 6°, 9°, and 12°, respectively. Figure 5(a) is from data using slice 1 in configuration 1 [Fig. 1(a)], where the telescope was fixed at 6°. The center of the slice here was at 0°.

The ringlike structures in Fig. 5 are reminiscent of those observed [7] in the case of the breakup of $^{20}$Ne and correspond to cuts of the sequentially forbidden sphere discussed above in the frame of the sequential breakup picture. The shifting of the position of the ring as the detection angle of the $^{12}$C changes in Fig. 5 can also be understood within the same sequential decay picture. Figure 5(d) corresponds to the case where the PLF detector was at 12° in configuration 2, well beyond the grazing angle (around 9° in this case). The inelastic scattering yield of primary $^{16}$O is expected [13] to concentrate at smaller angles. In the sequential breakup picture, $^{12}$C will be detected here mostly by emission of the alpha particle in the opposite direction, as observed experimentally.

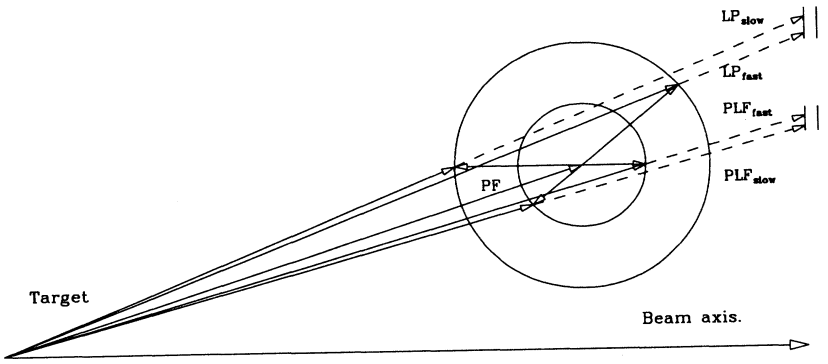


FIG. 4. Schematic representation of the velocity vectors involved in the sequential breakup of the PF. The limited acceptance of the PLF detector (trigger) imposes severe kinematical constraints on the direction and energy of the LP for a coincidence measurement.

The lowest threshold in $E_{\rm rel}$ is achieved when the heavy-ion telescope and the $\alpha$-particle detector are spatially close together. In our case this condition is met in configuration 1 when considering the cube-5–telescope pair. Figure 6 shows the $E_{\rm rel}$ spectrum resulting from coincidences between a $^{12}$C in the telescope and an $\alpha$ particle in cube 5. The dashed line shows the efficiency function as calculated by a simulation described below. The detection threshold in this case is below 1 MeV.

In this low $E_{\rm rel}$ region the yield is enhanced by the large efficiency, but remains small. The yield increases drastically above 2.4 MeV in a region where the detection efficiency is flat. Below 2.4 MeV some of the yield can be related to the breakup of $^{16}$O into $^{12}$C(4.4 MeV, 2+) + $\alpha$, which we cannot resolve in our $Q_3$ spectra. The excitation energy threshold for this channel to open is 11.6 MeV, and calculations of the branching ratio to this specific channel show that beyond 12 MeV of excitation, it is as large as that for the decay to the ground state of $^{12}$C.

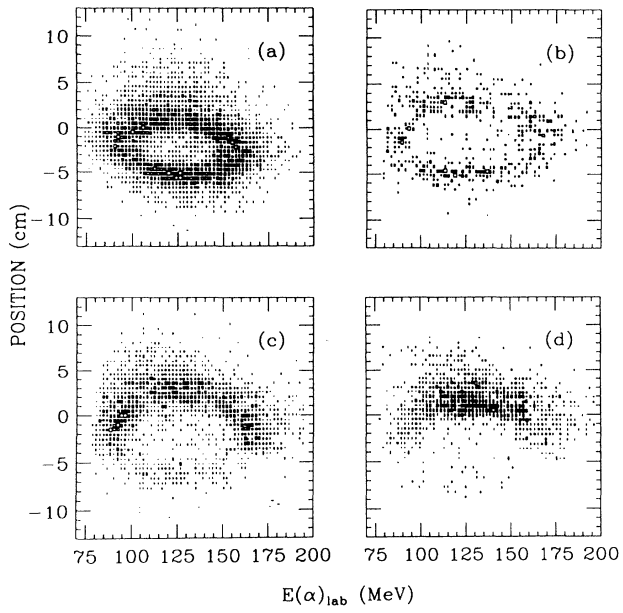


FIG. 5. Two-dimensional spectra of energy vs position along the long dimension of a slice, for alpha particles in coincidence with $^{12}$C. (a) Data taken with slice 1 of configuration 1; (b), (c), and (d) Data of configuration 2 with telescope 1 at 6°, 9°, and 12° (laboratory), respectively, and slice 2. All data correspond to events in the $Q_{ggg}$ peak. All frames show the ringlike structure characteristic of the sequential breakup mechanism. The disappearance of yield at large negative positions, when the telescope moves to larger angles, as well as the shifting of the ring, are features expected from the kinematics of sequential breakup.

Figure 7 shows, for this same close geometry, the $\alpha$ energy when it is in coincidence with a $^{12}$C. There are two groups which can be interpreted as the forward and backward emission of the $\alpha$ by $^{16}$O in a sequential breakup process. In the case of a sizable contribution from a direct breakup mechanism, the yield would be expected to fill in the space between the two groups, as found [14, 15] in the case of the breakup of $^{6,7}$Li.

The detailed study of the breakup of $^{16}$O into $^{12}$C + $\alpha$, where the signature of the sequential decay is the cleanest, yields no conclusive evidence for the existence of a direct breakup mechanism in competition with the sequential one.

A similar analysis of the $^{15}$N + $p$ channel cannot be carried out because of the lack of a distinct $Q_{ggg}$ peak in the corresponding $Q_3$ spectra. This lack, however, can also be understood qualitatively in terms of the sequential process: The threshold for proton emission in $^{16}$O is much higher than that for $\alpha$ emission (12.1 MeV vs 7.16 MeV [12]). On the other hand, statistical model calculations show that the alpha decay mode in $^{16}$O is the dominant one up to excitation energies around 24 MeV, where proton and alpha emission become comparable in intensity. To reach such high excitation energies in $^{16}$O one would require, on average, more violent collisions, resulting also in the production of enough excitation energy in the TLF to produce a $Q_3$ value beyond the region where we expect the quasielastic peak to appear. A more detailed study of this channel would be required to rule out the existence of contributions from direct processes to the $^{15}$N + $p$ yield.

## IV. MONTE CARLO SIMULATION

Since the main characteristics of the data are consistent with a two-step sequential process, we decided to de-

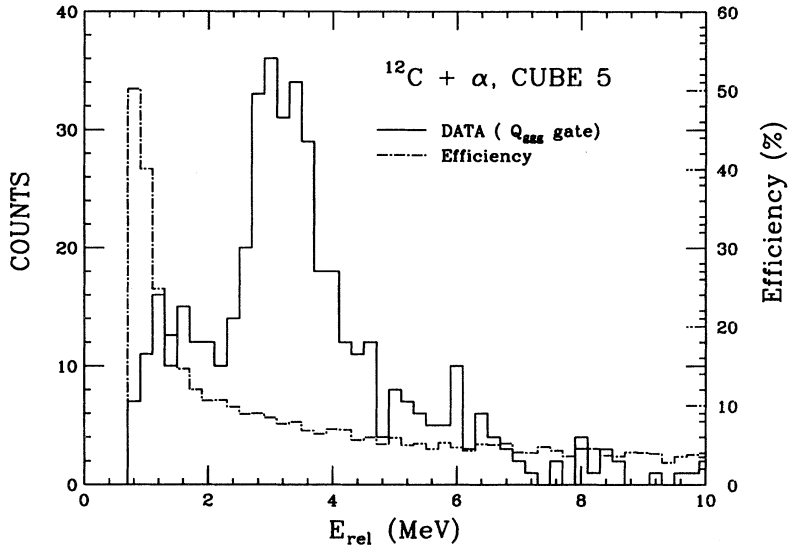


FIG. 6. Relative kinetic energy of the $\alpha$+$^{12}$C channel as measured using configuration 1, with cube 5 as the LP detector. The histogram shows data gated on the $Q_{ggg}$ peak. The dashed line shows the efficiency as a function of $E_{rel}$.

velop a Monte Carlo simulation program with two main objectives: (i) Perform a more detailed comparison between the data and the predicted behavior of a purely sequential process. Significant deviations would then indicate contributions from other mechanisms. (ii) Calculate the efficiency of our detection geometries in order to extract cross sections.

In the following we will describe briefly the main ingredients of such calculations as well as illustrate the level of agreement with the data.

### A. Primary fragment properties

Our simulation program has been developed as a simple way of taking into account the kinematical conditions of the reaction mechanism under the assumption that the whole process is a two-step (sequential) one. In the first step, the projectile interacts with the target, exchanging mass, excitation energy, and linear and angular momentum. A PF and a TLF are formed and the only relevant cases are those where the PF acquires enough excitation energy to be above the threshold of the channel in study (in the two cases we will present here, the $\alpha$ emission threshold of the PF). The underlying processes involved in the formation of the PF are assumed to be inelastic scattering for $^{16}$O and neutron pickup for $^{17}$O. The way in which the excitation energy is shared between the PF and TLF in the collision is a question subject to present study (see Ref. [9] and references therein), but will not be addressed in this work as we restrict ourselves to events where, by definition, the TLF is left relatively "cold." The simulation will treat excitation in both fragments as uncorrelated quantities event by event. The excitation energy distribution of the TLF will be taken to be a Gaussian with a width equal to the width of the $Q_{ggg}$ peak in the corresponding $Q_3$ spectrum.

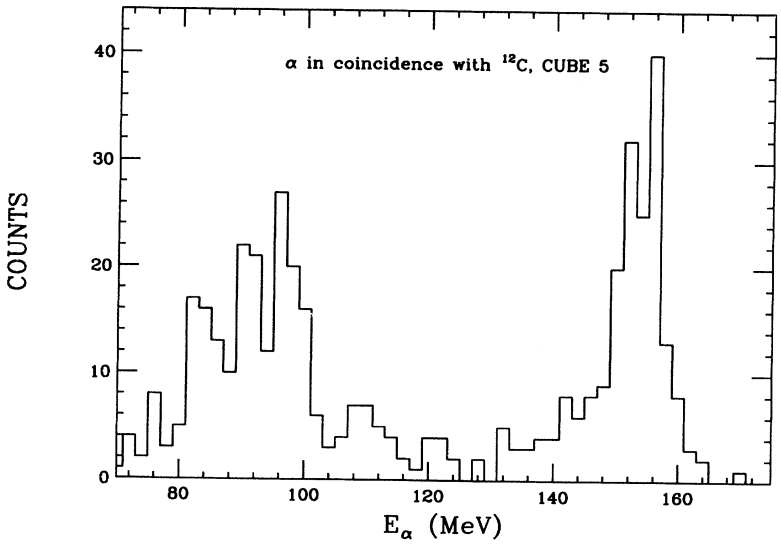


FIG. 7. Energy spectrum for alphas corresponding to the data shown in Fig. 6. The forward and backward solutions associated with sequential-decay kinematics are clearly visible.

### 1. *Excitation energy distributions*

In order to perform our simulations, we require input about the excitation energy generated in the primary fragment before breakup, the angle at which the PF is deflected, and finally the direction in which the light particle is emitted. All these quantities will be obtained from distributions which reflect the underlying assumptions of the reaction mechanism. In this section and the following we will discuss those distributions used in the simulation as input that yielded the best agreement with the data, in what we call "the most successful simulation." Since many features of the data can be examined simultaneously, there is no fitting procedure involved in the determination of the characteristics of these input distributions or other parameters involved in the simulation, but rather an overall judgement of the agreement between the calculated spectra and the data. A simulation was taken to be good when the relative kinetic spectra, the primary angular distributions (theta and phi), and the relative yields in all detectors in configuration 1 or configuration 2 were reproduced qualitatively. It is worth noting that, in order to do any comparison, the detection thresholds and detector resolutions were also simulated and the calculation "filtered" through them to produce experimental-like quantities.

Figures 8(a) and 8(b) show the relative kinetic-energy distribution used for $\alpha$+$^{12}$C and $\alpha$+$^{13}$C in the most successful simulation. As has been mentioned earlier, these distributions can be related to the excitation energy distribution of the PF by assuming that both PLF and LP were formed in their respective ground state. It should be kept in mind that the distributions used as input to the simulation would be only that fraction of a total excitation energy distribution decaying to the channel under consideration. In other words, these distributions can be thought of as the product of the excitation energy distribution generated in the PF with the corresponding branching ratio to the observed decay channels.

In the case of $^{16}$O breaking into $^{12}$C + $\alpha$ [Fig. 8(a)], the maximum of the input $E_{\rm rel}$ distribution lies in a region corresponding to states around 11.6 MeV of excitation in $^{16}$O known to $\alpha$ decay strongly [12, 16]. The distribution then falls off exponentially towards larger and smaller excitation energies ($E_{\rm rel}$ values). A simple exponential distribution could not be used throughout the entire range of relative energies since it resulted in a yield inconsistent with the measured one close to the threshold. An exponential falloff in this near-threshold region better fitted our data. In our sequential decay picture, this drop can be directly related to the fact that there are very few states available for breakup of $^{16}$O into $^{12}$C + $\alpha$ in this excitation energy region.

In the $^{17}$O case [Fig. 8(b)], the distribution used in the program for the $^{13}$C + $\alpha$ quasielastic data follows a spectral shape proposed by Padalino *et al.* [13] with a gamma parameter of 0.3.

According to the calculated branching ratios, using code STATIS [17], a large fraction of the $^{17}$O originally produced above 18 MeV will decay via channels other than $^{13}$C + $\alpha$. In particular, part of this $^{17}$O strength will appear as $^{12}$C + $\alpha$+ $n$, as evidenced in our $^{12}$C + $\alpha$ spectra, via sequential $n$-$\alpha$ or $\alpha$-$n$ decay. A prediction for the optimum $Q$ value ($Q_{\rm opt}$) [8] generates in the reaction a total excitation energy of about 23 MeV. Most of this excitation is expected to appear in the nucleus receiving the transferred nucleon [9]. The excitation energy distribution used as input for the simulation of the $^{13}$C + $\alpha$ channel that produces the best agreement with the data peaks at about 10 MeV [see Fig. 8(b)], showing what fraction of the total $^{17}$O produced we see through this channel: that with the lowest excitation energies. This illustrates how important four-body channels can be in the decay of $^{17}$O primarily produced in this reaction.

### 2. *Primary angular distributions*

In this section we will refer to angular distributions of the PF relative to the PF-TLF center-of-mass system, where the "$Z$" axis is defined by the projectile motion.

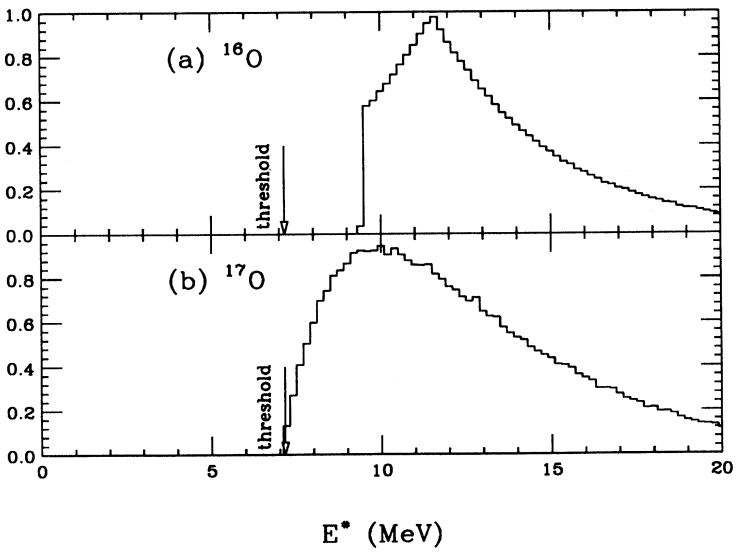


FIG. 8. Excitation energy distributions used as input to the Monte Carlo simulation for the (a) $\alpha$+$^{12}$C and (b) $\alpha$+$^{13}$C channels.

Azimuthal symmetry leaves us the freedom to chose the direction of the other two axes arbitrarily. We have chosen to define the "$Y$" axis as pointing up.

The direction of motion of the PF is determined by the properties of the scattering process. We have used one and the same polar angular distribution for all different values of excitation energy in the PF, which should then be regarded as a mean distribution. As we are dealing with unbound states, no previous information is available concerning these particular angular distributions. However, distorted wave Born approximation (DWBA) calculations [18] show that for inelastic scattering and one-neutron pickup, the shape of the distribution is not very sensitive to excitation energy and spin of the PF, except for oscillations in the small-angle region. Figure 9 (top panel) shows the angular distribution adopted for $^{16}$O in this work, which is not the result of any fitting procedure but rather of a DWBA calculation. The primary $^{17}$O angular distribution was assumed to have a Gaussian shape, whose centroid and width were adjusted to best fit the data. At a later stage this distribution was compared with a prediction of the diffraction model of Mermaz [19]. Figure 9 (bottom panel) shows that there is good agreement between them.

### B. Properties of the secondary emission

Once the PF's excitation energy and direction of motion have been determined, it will be allowed to decay. It is assumed that the PF lives long enough so that the breakup occurs far outside the region of strong interaction with the target, moving in a straight trajectory. We define the reaction plane as the one containing the beam and the PF velocity vectors.

$\alpha$ particles will be emitted by the PF ($^{16}$O or $^{17}$O) with an energy relative to the PLF ($^{12}$C or $^{13}$C) given by the distribution discussed above. The direction of emission of $\alpha$ particles is chosen in the simulation from polar and azimuthal angular distributions relative to a system of coordinate axes fixed in the emitter. The polar angle is measured relative to a $Z$-axis perpendicular to the reaction plane, parallel to the classical orbital angular momentum.

The azimuthal distribution in this coordinate system was always kept isotropic, but we were unable to reproduce the experimental relative coincidence yields in the different LP detectors using isotropic emission in this frame. Instead, we introduced a Gaussian out-of-plane distribution centered in the reaction plane and allowed its width to vary to fit the data.

Since the cubes lie in the same plane as the PLF detector in configuration 1 [see Fig. 1(a)], an in-plane enhancement will tend to increase the coincident yield in those detectors at the expense of the yield in the slices that lie in planes parallel to it. The $Q_{ggg}$ gated coincidence data show a ratio in yield of cubes to slices of 0.39 and 0.32 for $^{12}$C + $\alpha$ and $^{13}$C + $\alpha$, respectively. Furthermore the ratio of the yield between adjacent slices 3 and 2 in the same configuration 1 is 0.25 and 0.31, respectively. The data seem to indicate a stronger in-plane enhancement for $^{12}$C + $\alpha$ than for $^{13}$C + $\alpha$. However, the simulation shows that this ratio is also dependent on such other quantities as the relative kinetic-energy distribution and the primary angular distribution. In a situation where all distributions were kept fixed and changing only this in-plane distribution, we found that the simulation actually requires similar widths (equal enhancement) for the $^{13}$C + $\alpha$ channel relative to the $^{12}$C + $\alpha$ channel. This is illustrated in Fig. 10. Figure 10(a) shows results for the $^{12}$C + $\alpha$ channel. Figure 10(b) shows the results for the analysis of the $^{13}$C + $\alpha$ channel. The error bars associated with data and calculations are statistical. Isotropic emission corresponds to the case of a very large (infinite) width in the in-plane distribution, and is seen to be inconsistent with our data.

It should be noted that the cubes/slices and slice3/slice2 ratios, while different measures of anisotropy, are in qualitative agreement. This is most evident for the $^{13}$C + $\alpha$ channel, where both ratios constrain the anisotropy to $\Delta\theta_{\mathrm{FWHM}} \approx 45°$, a result also consistent with the $^{12}$C + $\alpha$ channel. (It was observed that the simulated cubes/slices ratio exhibited a greater sensitivity to changes in the width of the input distribution.)

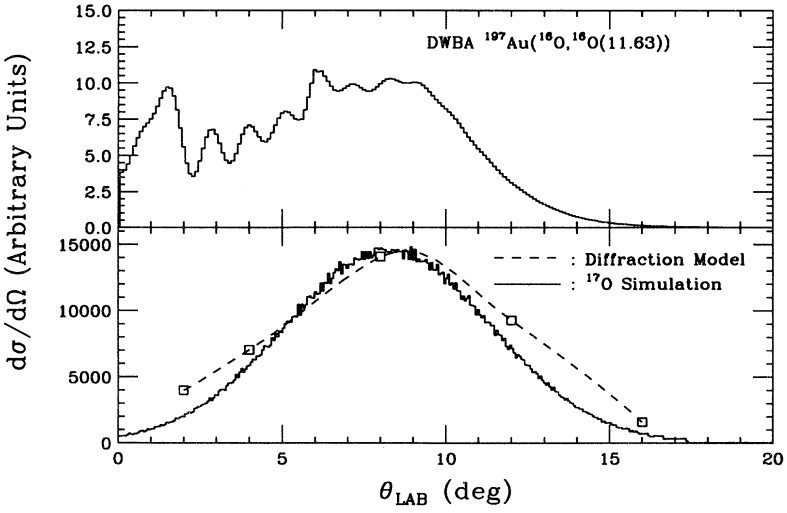


FIG. 9. Top panel: angular distribution for the inelastic scattering of $^{16}$O on $^{197}$Au to a state in oxygen at 11.63 MeV, as predicted by a DWBA calculation [18]. It was used as the primary angular distribution in the simulation of the $\alpha$+$^{12}$C channel. Bottom panel: the $\alpha$+$^{13}$C channel simulation was done using a Gaussian distribution centered at the classical grazing angle as input for the angular distribution of primary $^{17}$O. The histogram shows the distribution that best fits the data. The square symbols are predictions of a diffraction model [19], with a dashed line joining them to guide the eye.

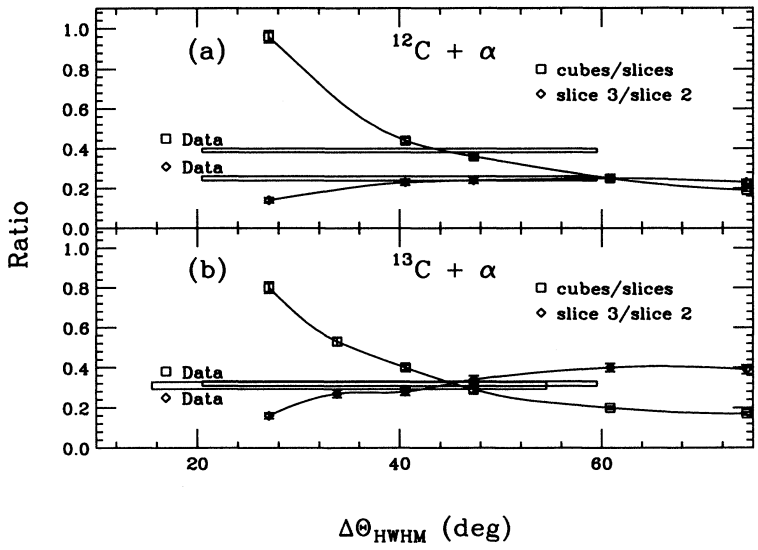


FIG. 10. On the horizontal axis is plotted the half width at half maximum of the Gaussian distribution used in the simulation to model the emission of alpha particles about the reaction plane. This plane is defined by the velocity vectors of the beam and the PF. The width is a measure of the coplanarity of the reaction. In each frame, two ratios are plotted: (i) the ratio of the summed yield in the cubes to that in the slices and (ii) the ratio of the yield in slice 2 to that in slice 3. All data are from configuration 1 and gated on the $Q_{ggg}$ peak. The bars show the experimental values of each ratio. Their widths correspond to the statistical error.

This effect may be interpreted as an indication of alignment with the angular momentum transferred in the reaction, and is consistent with the assumption that sequential breakup is the main underlying process in the formation of $^{12,13}$C PLFs.

### C. Comparison with the data

In this section we want to give some idea of the level of agreement that can be obtained between this simple Monte Carlo simulation program and the $Q_{ggg}$ gated data. To avoid repetition, we will show only comparisons with the $^{12}$C + $\alpha$ channel. The $^{13}$C + $\alpha$ channel, which also was simulated in detail, resulted in a similar agreement. Spectra obtained from configurations 1 and 2 were used to converge to what here will be presented as our most successful simulation.

Two spectra were found to better represent the overall agreement: (i) the $E_{\rm rel}$ spectrum and (ii) the polar angular distribution of the PF, as deduced from the PLF-LP coincidences.

Figure 11 shows a comparison of the polar angular distribution for primary $^{16}$O for configuration 2. Contributions from all LP detectors are included. The top panel shows the result when the PLF detector was at 12° in the laboratory. The bottom panel shows the case of the PLF detector at 9°. The overall shape of both distributions is well reproduced by the simulation, including the second peak at lower angles appearing at 9° relative to that at 12°. This structure is mostly due to the detection efficiency of our detector system.

Finally, Fig. 12 shows a histogram of the $E_{\rm rel}$ spectrum obtained with configuration 1, adding up the contribution of all LP detectors. In the same figure, the dots correspond to the equivalent spectrum resulting from the simulation.

With this sort of agreement we considered the simulation apt to provide a close estimation of our detection efficiency, for the reaction channels that were emulated.

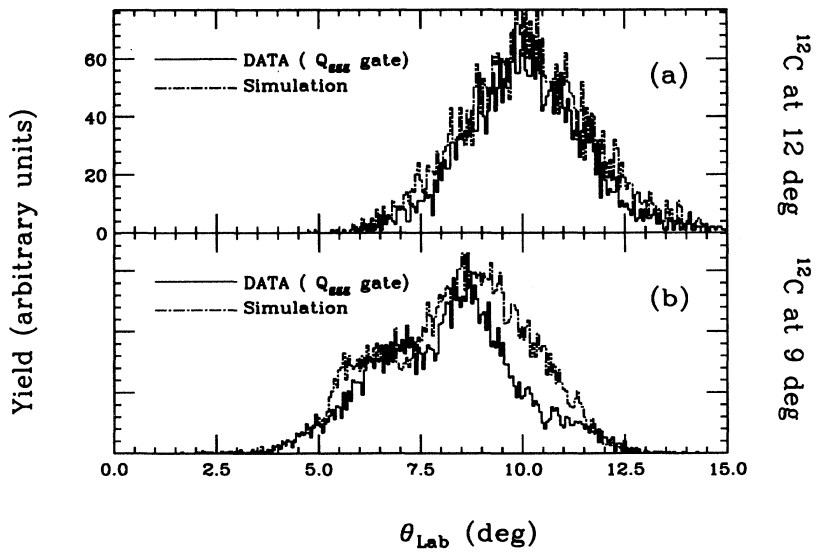


FIG. 11. Angular distributions of the PF as reconstructed from the $\alpha$+$^{12}$C coincidences. The data gated on $Q_{ggg}$ from configuration 2 with telescope 1 at 12° (top) and 9° (bottom) are shown with a solid line, the corresponding spectra obtained with the simulation are shown with a dot-dashed line. In both cases, contributions from all LP detectors are included.

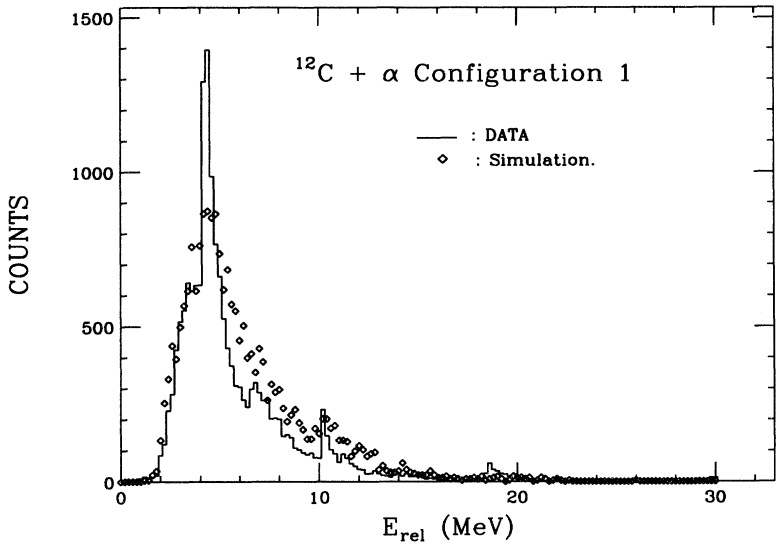


FIG. 12. The histogram shows the $Q_{ggg}$ gated $E_{rel}$ spectrum for the $\alpha$+$^{12}$C channel for configuration 1. All LP detectors are included. The symbols show the corresponding spectrum from the simulation.

### D. Efficiency-corrected reaction cross sections

Detection efficiencies were obtained from the simulation, and differential cross sections for $^{12}$C + $\alpha$, obtained after correction for efficiency, are given in Table IV.

Figure 13 shows the efficiency-corrected double-differential cross sections as a function of $E_{rel}$ (experimental configuration 1). The top spectrum corresponds to the case where contributions from all phoswiches have been added up, the middle and the bottom spectra where only contributions from slices closest to the target are considered. The integrals of the spectra agree to within 20%, indicating the magnitude of the uncertainties in our efficiency-corrected yields.

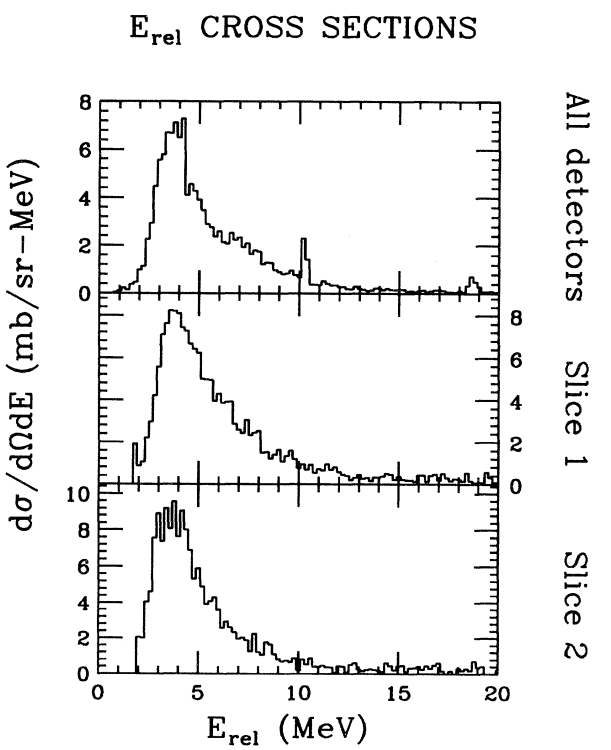


FIG. 13. Double-differential cross section for $\alpha$+$^{12}$C. The top frame is the result of correcting the $E_{rel}$ spectrum for efficiency. The other two frames show what would be obtained if the experiment had only slice 1 (middle) or slice 2 (bottom) from configuration 1, after correcting the associated spectra by the corresponding efficiency functions.

The angle-integrated cross sections for quasielastic $^{12,13}$C + $\alpha$ breakup were found to be 29 ± 6 mb and 16 ± 3.3 mb, respectively. These cross sections correspond to cases where the primary $^{16}$O and $^{17}$O fragments are produced in unbound states and decay by $\alpha$ emission to bound $^{12}$C and $^{13}$C states only. Therefore, they represent a fraction of the total $^{16,17}$O produced.

Another quantity of interest is the binary transfer cross section. $^{12}$C fragments produced via $\alpha$ transfer to the target will appear in events where there is a $^{12}$C but no LP in coincidence. We can, in principle, obtain this yield by subtracting the efficiency-corrected sum of all contributions from $^{12}$C detection in coincidence with 1, 2, or more LPs from the total inclusive yield. Using results from Table I and the cross sections given in the paragraph above, we find that only 13% of the inclusive $^{12}$C yield is produced by quasielastic breakup induced by inelastic scattering to unbound states. Assuming that the detection efficiency does not change drastically as a function of $Q_3$ (which is confirmed by our simulation as long as the reaction mechanism remains the same), and noting that the quasielastic peak represents only about 25% of the total $Q_3$ spectra, the $^{12}$C + $\alpha$ coincidence yield with all $Q_3$ values included (116 ± 24 mb) accounts for

TABLE IV. Differential cross sections (mb/sr).

| PLF angle (deg) | 4.5 | 6 | 6[a] | 9 | 12 | 16[b] |
|---|---|---|---|---|---|---|
| $^{12}$C+$\alpha$ | 214 | 189 | 136 | 82 | 25 | 1.5 |

[a]Data from configuration 1.
[b]Data from telescope 2.

TABLE V. Relative cross sections (arb. units).

| | |
|---|---|
| $^{12}$C+$\alpha$ | 216 |
| $^{12}$C+$\alpha$ ($Q_{ggg}$ only) | 65 |
| $^{12}$C+$\alpha$ + $n$ (see text) | 47 |
| $^{13}$C+$\alpha$ ($Q_{ggg}$ only) | 37 |
| $^{15}$N+$p$ | 117 |

about 50% of the inclusive one.

From Table II one can see that the largest contribution is from $^{12}$C + $\alpha$ coincidences. While all other channels are much weaker, our detection efficiency is also smaller. Our same simulation program can be used to estimate the efficiency for the detection of protons in coincidence with $^{12}$C if we make some suitable assumptions for the excitation energy in the parent ($^{13}$N) nucleus and all the distributions that enter the calculation. The result calls for a similar overall efficiency for $^{12}$C + $p$ as for $^{12}$C + $\alpha$. Neglecting possible existing correlations between the light particles sequentially emitted, the overall efficiency for the detection of two charged particles can be approximated by the product of their individual ones. Proceeding with this exercise, we estimate that the contribution from all other coincidence patterns (40 ± 20 mb) is about 20% of the inclusive one. As a result of this, our estimation of the total yield of $^{12}$C in coincidence with one or more LP is 156 ± 44 mb, to be compared with the 220 ± 44 mb of the inclusive yield from Table I. $\alpha$ transfer should then account for the difference. In other words, our measurements are consistent with a cross section of the order of 60 mb for $\alpha$ transfer from $^{16}$O to $^{197}$Au at this energy. The error bars would extend down to 0 and up to 142 mb. Given the experimental uncertainties, no conclusion can be reached concerning the importance of $\alpha$ transfer in this reaction.

To illustrate the relative importance of the different processes involved in the production of $^{12}$C and $^{13}$C PLFs, Table V compares the various cross section at 6° in experimental configuration 1. The $^{12}$C + $\alpha$ + $n$ yield (column "C") was obtained by subtracting the $^{13}$C + $\alpha$ $Q_3$ spectrum from the corresponding one for $^{12}$C + $\alpha$, after normalizing the yields in the $Q_{ggg}$ peaks (see Fig. 3). The numbers in the table show that the contribution to the $^{12}$C + $\alpha$ channel from the breakup of primary $^{17}$O $\rightarrow$$^{12}$C + $\alpha$ + $n$ with the neutron undetected is actually larger (some 25%) than to the quasielastic $^{17}$O $\rightarrow$$^{13}$C + $\alpha$ channel.

## V. CONCLUSIONS

Our simulation based on sequential breakup accounts for almost all observed details of the quasielastic data. In the initial stage, a PF is formed in an unbound state by low energy mechanisms such as inelastic scattering and one-neutron pickup. In a second stage, the PF decays statistically, leading to the formation of the detected LP and PLF. We could not find any evidence for a significant direct breakup component in the data. We showed, also, that our experimental setup, although not a $4\pi$ device, can be used to make quantitative studies about the relative importance of the various reaction mechanisms involved in PLF production, provided that the detection efficiency is calculated carefully.

The anisotropic emission of $\alpha$ particles about the reaction plane, found in this experiment, has been interpreted in terms of the alignment of the angular momentum transferred in the first step of the breakup process. We found that breakup of $^{17}$O, induced by neutron pickup, and that of $^{16}$O, induced by inelastic scattering, produced similar anisotropies.

Differential and angle-integrated cross sections for the quasielastic breakup of $^{16}$O (induced by inelastic scattering) and $^{17}$O (one-neutron pickup) were given, showing that this latter process plays a very important role in the breakup of the projectile.

## ACKNOWLEDGMENTS

We want to acknowledge the 88-Inch Cyclotron staff for the magnificent beams provided during the experiment, and Professor M. C. Mermaz for enlightening discussions, help in performing DWBA calculations, and more. This work was supported by the Division of Nuclear Physics of the U.S. Department of Energy under Contract No. DE-AC03-76SF00098. Three of us (E.C., A.D., and M.E.O.) want to acknowledge partial economic support from CONACYT. One of us (S.B.G.) acknowledges support from the National Science Foundation Presidential Young Investigator Program.

[1] S. Wald, S. B. Gazes, C. R. Albiston, Y. Chan, B. G. Harvey, M. J. Murphy, I. Tserruya, and R. G. Stokstad, Phys. Rev. C **32**, 894 (1985).
[2] R. Stock, Phys. Rep. **135**, 259 (1986).
[3] R. G. Stokstad, Comments Nucl. Part. Phys. **13**, 23 (1984).
[4] C. K. Gelbke, C. Olmer, M. Buenerd, D. L. Hendrie, J. Mahoney, M. C. Mermaz, and D. K. Scott, Phys. Rep. **42C**, 311 (1978).
[5] M. Bantel, R. G. Stokstad, Y. D. Chan, S. Wald, and P. J. Countryman, Nucl. Instrum. Methods **A226**, 394 (1984).
[6] H. R. Schmidt, M. Bantel, Y. Chan, S. B. Gazes, S. Wald, and R. G. Stokstad, Nucl. Instrum. Methods **A242**, 111 (1985).
[7] S. B. Gazes, H. R. Schmidt, Y. Chan, E. Chavez, R. Kamermans, and R. G. Stokstad, Phys. Rev. C **38**, 712 (1988).
[8] J. Wilczynski, K. Siwek-Wilczynska, J. Van Driel, S. Gonggrijp, D. C. J. M. Hageman, R. V. F. Janssens, J. Lukasiak, R. H. Siemssen, and S. Y. Van Der Werf, Nucl. Phys. **A373**, 109 (1982).
[9] J. Wilczynski and H. W. Wilschut, Phys. Rev. C **39**, 2475 (1989).
[10] J. Wilczynski and K. Siwek-Wilczynska, Phys. Rev. C **41**, R1917 (1990).

[11] S. B. Gazes, Y. D. Chan, E. Chavez, A. Dacal, M. E. Ortiz, K. Siwek-Wilczynska, J. Wilczynski, and R. G. Stokstad, Phys. Lett. B **208**, 194 (1988).
[12] F. Ajzenberg-Selove, Nucl. Phys. **A460**, 1 (1986).
[13] S. J. Padalino, R. A. Parker, and L. C. Dennis, Phys. Rev. C **33**, 1805 (1986).
[14] A. C. Shotter, A. N. Bice, J. M. Wouters, W. D. N. Rae, and J. Cerny, Phys. Rev. Lett. **46**, 12 (1981).
[15] A. C. Shotter, V. Rapp, T. Davinson, and D. Branford, Phys. Rev. Lett. **53**, 1539 (1984).
[16] W. D. N. Rae, A. J. Cole, B. J. Harvey, and R. G. Stokstad, Phys. Rev. C **30**, 158 (1984).
[17] R. G. Stokstad, Yale University WNSL Report No. 53, 1974 (unpublished).
[18] M. C. Mermaz, private communication.
[19] M. C. Mermaz, Phys. Rev. C **36**, 1000 (1987).